J. Fluid Mech. (2026), *vol.* 1031, A5, doi:10.1017/jfm.2026.11282

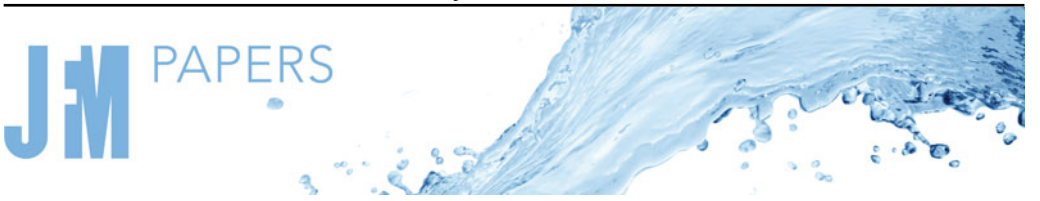

Bridging advection and diffusion in the encounter dynamics of sedimenting marine snow

Jan Turczynowicz[1,3], **Radost Waszkiewicz**[2,3], **Jonasz Słomka**[4] and **Maciej Lisicki**[1]

[1]Faculty of Physics, University of Warsaw, Pasteura 5, 02-093 Warsaw, Poland

[2]Institute of Physics, Polish Academy of Sciences, Aleja Lotnikow 32/46, PL-02668 Warsaw, Poland

[3]Fenix Science Club, Aleja Stanów Zjednoczonych 24, 03-964 Warsaw, Poland

[4]Institute of Environmental Engineering, Department of Civil, Environmental and Geomatic Engineering, ETH Zurich, Zurich, Switzerland

Corresponding authors: Maciej Lisicki, mklis@fuw.edu.pl; Jonasz Słomka, jslomka@ethz.ch

(Received 18 September 2025; revised 12 December 2025; accepted 28 January 2026)

Sinking marine snow particles, composed primarily of organic matter, control the global export of photosynthetically fixed carbon from the ocean surface to depth. The fate of sedimenting particles is partly regulated by their encounters with suspended objects, which leads to mass accretion and potentially alters their buoyancy, and with bacteria that can colonise the particles and degrade them. Their collision rates are typically calculated using two types of models focusing either on direct (ballistic) interception with a finite interaction range, or advective-diffusive capture with zero interaction range. Yet, since many relevant marine encounter scenarios span across both regimes, quantifying such encounters remains challenging because the two models yield asymptotically different predictions at high Péclet numbers. We reconcile the two approaches by quantifying encounters in the general case using theoretical analysis and simulations. By solving the advection-diffusion equation in Stokes flow around a sphere to model mass transfer to a sinking particle by finite-sized objects, we determine a new formula for the Sherwood number as a function of the Péclet number and the ratio of particle sizes. Contrary to the common assumption, we find that diffusion still plays a significant role in generating encounters even at high Péclet numbers. We predict that at Péclet numbers as high as 10^6 the direct interception model underestimates the encounter rate by up to two orders of magnitude. This overlooked contribution of diffusion to encounters suggests that processes affecting the fate of marine snow may proceed at a rate much higher than previously thought.

Key words: ocean processes, sediment transport, coupled diffusion and flow

1. Introduction

The oceans play a central role in capturing anthropogenic CO_2, primarily through dissolution processes, resulting in a significant portion of it being stored within seawater (Broecker & Peng 1982; Sabine *et al.* 2004; Sarmiento & Gruber 2006). A fraction of the dissolved CO_2 is transformed into organic compounds by the photosynthetic activity of phytoplankton (Guidi *et al.* 2016) dwelling in the well-mixed euphotic zone, which extends from the surface to a depth of approximately 100 m (Buesseler & Boyd 2009; Buesseler *et al.* 2020), and then is further converted into particulate matter known as marine snow. Marine snow particles form through aggregation of dead or senescent cells, detritus, organic and inorganic matter, and span many orders of magnitude in size and sinking speed (Duret 2018; Cael *et al.* 2021; Clements *et al.* 2022; Williams & Giering 2022). Some of them sink beneath the mixing layer and start a journey to depth through mostly quiescent waters. This sedimentation-driven process (and, to a lesser extent, active transport by migrating organisms at intermediate depth (Boyd *et al.* 2019)), called the biological carbon pump, is a significant mechanism of CO_2 sequestration on the seabed (Sarmiento & Gruber 2006; Boyd *et al.* 2019). Field observations, described by the Martin curve (Martin *et al.* 1987), show that as little as 10 % of the carbon sediment reaches depths beyond 200 m below the euphotic zone (Buesseler & Boyd 2009), and the carbon flux decays rapidly with depth (Buesseler *et al.* 2007; Olli 2015; Smith *et al.* 2018; Armstrong *et al.* 2001; Giering *et al.* 2017; Laufkötter *et al.* 2017; Middelburg 2019; Jang *et al.* 2024; Marsay *et al.* 2015; Takeuchi, Giering & Yamazaki 2024). Quantification of this flux decay requires understanding of the underlying microscale interactions within sedimenting matter (Nguyen *et al.* 2022).

The drivers of vertical mass transport in the deep ocean, below the euphotic zone, include (DeVries, Liang & Deutsch 2014; Omand *et al.* 2020): sedimentation of a heterogeneous ensemble of particles (Kajihara 1971; Chase 1979; Iversen *et al.* 2010; Chajwa *et al.* 2024), particle remineralisation responsible for mass loss (Iversen & Ploug 2013; Lambert, Fernandez & Stocker 2019; Alcolombri *et al.* 2021; Kiørboe *et al.* 2002; Nguyen *et al.* 2022; Anderson *et al.* 2023;), mass gain due to aggregation (Jackson 1990; Kriest & Evans 2000; Gehlen *et al.* 2006; Burd & Jackson 2009) and fragmentation by multiple mechanisms (Briggs, Dall'Olmo & Claustre 2020; Dilling & Alldredge 2000). Most of these processes are influenced, at least in part, by particle collisions. For example, the number of bacteria that colonise a particle can be affected by encounters with free-living populations (Kiørboe *et al.* 2002; Nguyen *et al.* 2022), increasing their degradation. Collisions with neutrally buoyant gels can decrease the density of a particle (Alcolombri *et al.* 2025), reducing its sinking speed. On the other hand, encounters with smaller marine snow particles can increase the sedimentation speed through mass accretion (Burd & Jackson 2009). These examples highlight an important class of collisions that significantly influence the fate of marine snow particles: encounters between a large particle and small suspended objects.

As a paradigm model of encounters, researchers typically consider marine snow as a spherical particle that undergoes Stokesian sedimentation and intercepts suspended objects (Friedlander 1957; Jackson 1990; Kiørboe & Titelman 1998; Kiørboe *et al.* 2001; Humphries 2009; Burd & Jackson 2009). The encounter rate in such systems has been calculated using two distinct approaches. The first approach focuses on a direct or ballistic interception with a finite interaction range (Kiørboe & Titelman 1998; Humphries 2009). This model accounts for the non-negligible size ratio of the encountered objects and is primarily used for particles with high sinking speeds because it neglects the effects of diffusion of the objects. The second model is based on the advection-diffusion equation, and

while it accounts for diffusion and flow around a sphere, it assumes a zero interaction range (i.e. a negligible effective size of the suspended objects) (Friedlander 1957; Clift, Grace & Weber 2013; Kiørboe *et al.* 2001; Karp-Boss, Boss & Jumars 1996). This model works well for determining the concentration and flux of oxygen onto a large particle colonised by bacteria, as established both experimentally and theoretically (Kiørboe & Thygesen 2001). However, the validity of either approach is unclear in intermediate scenarios, when the size of the objects becomes significant and their diffusion cannot be neglected. Furthermore, the two models yield asymptotically divergent predictions depending on how the size and speed of the sinking particle and the size of the intercepted objects are varied. Consequently, it is challenging to quantify encounter scenarios in marine snow particles accurately because the particles span many orders of magnitude in size and sinking speed. Moreover, they can collide with objects that can be both diffusive and have a finite interaction length (e.g, bacteria, gels or other smaller marine snow particles).

Here, we quantify encounters between sinking marine snow and suspended objects as a function of four key parameters: the size and sinking speed of the marine snow and the size and diffusivity of the objects. We determine the correct asymptotics of the encounter rate of fast-sedimenting particles, reconciling the advection-diffusion model with the direct interception model. Our model provides a practical, closed-form formula for the encounter rate between a large sinking particle and suspended objects. Our results suggest that the number of collisions between picoplankton and larger particles may have been underestimated by the direct interception model, even by two orders of magnitude.

The structure of the article is as follows. First, in § 2, we provide an outline of physical processes involved in marine snow encounters, along with representative examples of collision scenarios which warrant theoretical quantification. In § 3, we present the key equations that describe encounters and define the theoretical framework. We discuss the asymptotic solutions in § 4, before performing the analysis of numerical solutions in § 5.1. Based on the results, in § 5.2 we present a closed-form approximation for the encounter kernel valid for intermediate collision scenarios. We discuss the relevance of the kernel for marine snow in § 6, where we set our results in the context of pico- and nanoplankton encounters. In the following § 7, we discuss the limitations and opportunities that our approach provides. We conclude the paper in § 8.

2. Qualitative collision mechanisms

The nature of encounters between marine snow and suspended objects ranges from purely diffusive to purely ballistic, because marine snow particles are highly heterogeneous (Trudnowska *et al.* 2021), and cover a wide range of sizes and sinking speeds. The size of marine snow particles varies in the range of 1 μm to several millimetres (McDonnell & Buesseler 2010; Bochdansky, Clouse & Herndl 2016; Williams & Giering 2022), as visible in figure 1(*a*), with sedimentation speeds from zero to several hundreds of metres per day (Williams & Giering 2022). For most particles, the Reynolds number Re is less than unity (Kiørboe *et al.* 2001; Alldredge 1998). Thus, the Stokes approximation provides a suitable starting point, as confirmed by recent measurements (Chajwa *et al.* 2024) of flow fields around sinking marine snow, shown in figure 1(*b*).

We qualitatively describe a collision of two particles moving with relative velocity U and diffusion constant D considering two dimensionless numbers. With a denoting the effective radius of the larger particle and b the interaction range between the smaller and the larger particle (such that whenever the centres of the particles are at most $a + b$ apart they collide), we define the Péclet number Pe and β describing the size ratio of the

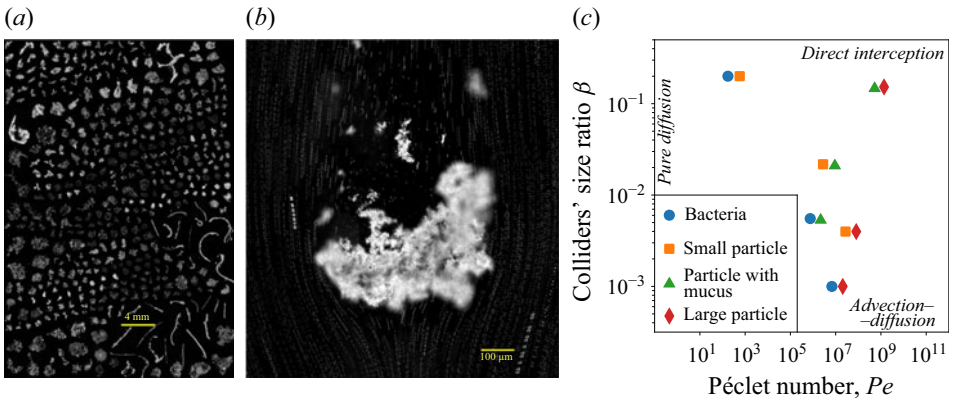

Figure 1. The landscape of collision types in marine snow indicates the different physical encounter mechanisms at play. (*a*) Examples of different sizes and shapes of marine aggregates, imaged *in situ* off the coast of East Greenland. Image courtesy of E. Trudnowska, Polish Academy of Sciences. (*b*) Sample image of a marine snow particle collected at 80 m below sea level, with the flow field visualised by plastic microbeads. Image by R. Chajwa *et al.*, CC BY 4.0 (Chajwa *et al.* 2023). (*c*) Archetypal collision types between different objects (symbols) in the parameter space of the Péclet number Pe and relative size β, based on experimental data in table 1. Possible collision types cover the whole space, ranging qualitatively from purely diffusive encounters, through advective-diffusive encounters, to direct (ballistic) interception. Existing collision models account for the limiting cases only.

Particle or object type	Radius (µm)	Sinking rate (m day^{-1})	Diffusion coefficient (µm^2 day^{-1})
Large particle (Iversen & Ploug 2010)	1000	130	11
Medium-sized, mucus laden particle (Chajwa *et al.* 2024)	190	78	58
Small particle (Chase 1979)	4	1	2 700
Non-motile bacterium (Kiørboe *et al.* 2002)	1	0	11 000

Table 1. Selected representative examples of particulate matter involved in marine snow encounters, with their typical size and sinking speed as reported in experimental observations and calculated the diffusion coefficient using the Stokes–Einstein relationship (assuming viscosity of seawater to be $\mu = 1.6 \times 10^{-3}$ Pa s). When calculating β and Pe for a pair, we assumed that the interaction range b is the radius of a smaller particle and that the diffusion coefficient is a sum of individual diffusion coefficients.

colliders as

$$Pe = \frac{U(a+b)}{D}, \qquad \beta = \frac{b}{a+b}. \tag{2.1}$$

To estimate the possible values of the two parameters, we consider four illustrative actors: a small marine snow particle (smallest measured particles (McCave 1984)); a medium-sized, mucus-laden particle (Chajwa *et al.* 2024); a large particle (around the 10th particle mass quantile (Iversen *et al.* 2010)); and a non-motile bacterium (Kiørboe *et al.* 2002). This set covers a broad range of possible collision parameters, outlined in table 1. An estimate of Pe and β for collisions between them is shown in figure 1(*c*), confirming that both β and Pe span several orders of magnitude.

For very small values of Pe, diffusion dominates the encounter rate. In this scenario, collisions can be viewed as stochastic, where the large, slowly sedimenting particle 'bumps into' smaller particles. We refer to this collision mode as purely diffusive. When the

colliders' size ratio, β, is vanishingly small but Pe becomes significant (e.g. 10^6), advection can transport new particles into the depleted region. In this way, the sedimenting particle 'bumps into' more particles, although the encounter mechanism remains diffusive as there is no slip at the particle surface. We refer to this collision mode as advection-diffusion. On the right-hand side of figure 1(*c*), for very large values of Pe (e.g. 10^9) and a non-negligible size ratio, β (e.g. 10^{-2}), previous studies have assumed that the diffusion of the smaller particle becomes negligible. In such cases, collisions can be conceptualised as a large, rapidly sedimenting particle 'sweeping away' stationary smaller particles. We refer to this collision mode as direct interception.

A natural question arises concerning the range of applicability of these models. This question escapes a simplistic answer, because only the limiting cases have been analysed so far. Without a quantitative model of the encounter rate, valid across a broad range of Pe and β, assuming one limiting case over another may severely underestimate the encounter rates. We develop tools to resolve this tension in the remainder of this article.

3. Governing equations

Consider a sphere of radius a sedimenting with a velocity U in a quiescent fluid. In the Stokesian regime and for an incompressible fluid, the velocity field in cylindrical coordinates (ρ, θ, z), with $\boldsymbol{U}$ aligned with the z axis, is given by $\boldsymbol{u} = (u_\rho, u_z)$. The velocity components and the corresponding streamfunction ψ expressed in the sphere frame of reference, are given by (Landau & Lifshitz 1987)

$$u_\rho = \frac{3a\rho z U}{4R}\left(\left(\frac{a}{R^2}\right)^2 - \frac{1}{R^2}\right), \tag{3.1}$$

$$u_z = U + \frac{3aU}{4R}\left(\frac{2a^2+3\rho^2}{3R^2} - \left(\frac{\rho a}{R^2}\right)^2 - 2\right), \tag{3.2}$$

$$\psi = \frac{1}{2}\,U\,\rho^2\left(1 - \frac{3}{2}\frac{a}{R} + \frac{1}{2}\left(\frac{a}{R}\right)^3\right), \tag{3.3}$$

$$R^2 = \rho^2 + z^2. \tag{3.4}$$

The streamlines of the flow field around the particle are visualised in figure 2(*a*). Suppose now that the suspending fluid contains small objects of effective radius b which undergo diffusion relative to the large particle, with a diffusion coefficient D. Whenever the distance between the centre of a small object and the centre of the sphere is smaller than $a + b$, the objects stick to the sphere and are removed from the surrounding liquid. This process can model direct contact of small spherical objects with a larger particle, but different capture mechanics can also be modelled in this fashion; one possibility is an electrostatic attraction between the particle and a small object with an effective interaction range b (which can be derived by comparing the interaction potential with the typical energy of thermal fluctuations, $k_B T$) (Zaccone *et al.* 2010). Alternatively, in the case of slip or mixed boundary conditions on the sedimenting sphere, an effective Stokes radius a can be introduced and the difference between the true size and the Stokes size would give the effective interaction size. In these cases, $\beta = 0.2$ would cover, for example, the case where the large collider has the Stokes radius $a = 100\,\mu\text{m}$, and the effective collision radius of 115 μm (e.g. due to its porous nature), and it collides with a solid sphere of size 5 μm giving $b = 20\,\mu\text{m}$, while at the same time introducing only a small perturbation to the flow field. Regardless of the specific origin of such interaction range, we focus here on the consequences of a finite interaction range described by b. We further assume that the captured particles are much smaller than the sedimenting sphere, so that their influence

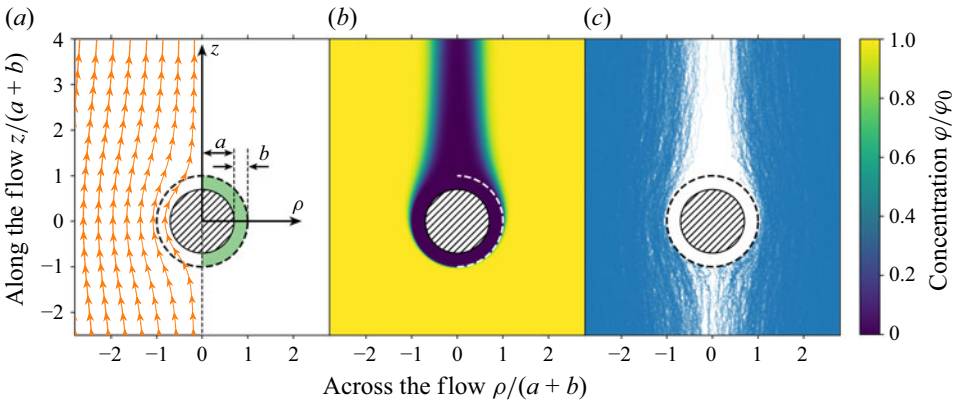

Figure 2. Sedimenting Stokesian sphere colliding with Brownian objects with a non-zero interaction range. (*a*) Geometry of the collisions. Stokes flow streamlines around a particle of radius a representing sedimenting marine snow, with an interaction range b marked in green. The interaction radius accounts for the finite size of the suspended objects. Given the axial symmetry, we introduce sideways (ρ) and downstream (z) coordinates to parametrise the system. (*b*) Numerical solution of the advection-diffusion equation obtained using the finite element method for the steady concentration field around a sedimenting sphere (dashed area) with a size ratio $\beta = 0.2$ (dashed line) at $Pe = 500$. (*c*) Stochastic trajectories of objects obeying the advection-diffusion equation at $Pe = 500$. Here, $N = 3 \times 10^3$ trajectories of objects were initially distributed uniformly on a large disk upstream of the sphere (thus more numerous further from the axis of symmetry). Trajectories that collided with the enlarged sphere (dashed) are terminated, leading to the formation of a characteristic wake free of objects behind the sphere. Note: the decreased number of trajectories upstream, at the centre, is caused by accumulating simulations in three dimensions to ρ and z. Thus a spatially uniform distribution transforms to a linearly increasing one, $2\pi\rho\,\mathrm{d}\rho$.

on the flow field around the large sphere can be neglected. In this case, the steady state concentration profile of small particles φ is governed by the advection-diffusion equation (Kiørboe & Thygesen 2001)

$$0 = D\nabla^2\varphi - \boldsymbol{u}\cdot\nabla\varphi, \tag{3.5}$$

with the boundary condition of constant concentration, $\varphi = \varphi_0$, upstream of the ball, and $\varphi = 0$ on a sphere with an effective radius of $a + b$. To make (3.5) dimensionless, we choose the time scale to be $(a+b)/U$, use $a+b$ as the length scale and φ_0 as the concentration scale and arrive at the dimensionless form

$$0 = \nabla^2\varphi - Pe\,(\boldsymbol{u}\cdot\nabla\varphi), \tag{3.6}$$

with the boundary conditions for concentration

$$\begin{aligned} \varphi(r=1) &= 0, \\ \varphi(r\to\infty) &= 1. \end{aligned} \tag{3.7}$$

The dimensionless velocity field, (3.1)–(3.2), can be written in terms of the rescaled large particle radius $\alpha = a/(a+b)$ as

$$\begin{aligned} u_\rho &= \frac{3\alpha\rho z}{4R}\left(\left(\frac{\alpha}{R^2}\right)^2 - \frac{1}{R^2}\right), \\ u_z &= 1 + \frac{3\alpha}{4R}\left(\frac{2\alpha^2+3\rho^2}{3R^2} - \left(\frac{\rho\alpha}{R^2}\right)^2 - 2\right). \end{aligned} \tag{3.8}$$

Crucially, the boundary conditions of no slip and no concentration are imposed here on different surfaces, with $\boldsymbol{u}(r=\alpha) = 0$, rather than the classical case, where $\boldsymbol{u}(r=1) = 0$.

We now calculate the mass of small particles intercepted by the large particle per unit time. Expressing (3.6) as $0 = \nabla \cdot \boldsymbol{J}$, we can write the particle current $\boldsymbol{J}$ as

$$\boldsymbol{J} = Pe\, \boldsymbol{u}\varphi - \nabla\varphi, \tag{3.9}$$

where we used the fact that the flow is incompressible, $\nabla \cdot \boldsymbol{u} = 0$. The total, dimensionless flux of particles onto the sphere, Φ^*, is given by

$$\Phi^* = \oint_{sphere} \boldsymbol{J} \cdot \mathrm{d}\boldsymbol{S}. \tag{3.10}$$

Using the Stokes theorem, and given the lack of source terms in (3.6), the integration surface in (3.10) can be changed to any other surface enclosing the sphere. When the integration surface is taken as a large cylinder that extends far from the sphere, we have $\partial_z\varphi \ll \boldsymbol{u}\varphi$, and we can avoid calculating the gradient in the numerical evaluation of $\boldsymbol{J}$. The dimensional flux is calculated as $\Phi = \varphi_0 D(a+b)\Phi^*$. With precise definitions, we are ready to discuss different approximations used to compute Φ for given values of Pe and β.

4. Divergent asymptotics of the limiting cases

Before solving (3.6) in the most general case ($Pe \geqslant 0$, $\beta \geqslant 0$), we first briefly discuss its important limiting cases, namely the widely used direct interception limit and the advection-diffusion description with a zero interaction range. We also highlight important scenarios under which these limiting cases break down and yield asymptotically divergent predictions.

In the absence of flow ($Pe \to 0$, purely diffusive encounters), (3.6) becomes a spherically symmetric Laplace's equation, giving the classical expression for the diffusive flux Φ_D onto a sphere (Karp-Boss *et al.* 1996)

$$\Phi_D = 4\pi\, D(a+b)\varphi_0. \tag{4.1}$$

When flow is present ($Pe > 0$, advective-diffusive encounters) it is customary to normalise Φ by this limiting case to obtain the dimensionless quantity proportional to the encounter rate. This ratio defines the Sherwood number (Karp-Boss *et al.* 1996), given by

$$Sh = \frac{\Phi}{\Phi_D}. \tag{4.2}$$

Note that there is no consensus on the definition of Sh and Pe in the literature and the definitions might differ by a factor of two.

For an arbitrary value of Pe and in the limit of a zero interaction range ($\beta \to 0$), (3.6) also describes heat transfer to or from a sphere in a slowly flowing fluid. In the limit of small or high Péclet number, analytical solutions of this problem were obtained using perturbative methods (Acrivos & Taylor 1962; Acrivos & Goddard 1965; Rimmer 1968; Gupalo & Ryazantsev 1972; Brunn 1982; Bell *et al.* 2013). Intermediate cases require numerical simulations, pursued since the early work of Friedlander (1957). To date, numerical solutions of heat transfer between a sphere immersed in a colder, flowing liquid are well established (Westerberg & Finlayson 1990; Feng & Michaelides 2000; Clift *et al.* 2013), and a simple, closed-form approximation of numerical results provided by Clift *et al.* (2013) gives the Sherwood number Sh_{Cl} in terms of Pe with great accuracy, up to 2 %,

for the entire range $0 \leqslant Pe < \infty$

$$Sh_{Cl} = \frac{\Phi_{Cl}}{\Phi_D} = \frac{1}{2}\left(1 + (1+2Pe)^{1/3}\right) = \frac{1}{2} + \left(\frac{1}{8} + \frac{Pe}{4}\right)^{1/3}. \tag{4.3}$$

These are in agreement with experimental results considering a heated sphere in slowly flowing fluid (Kramers 1946) and absorption of ions by a conducting sphere (Kutateladze, Nakoryakov & Iskakov 1982). However, we stress that all of these approaches assume a zero interaction range $\beta \to 0$.

When advection dominates over diffusion (i.e. diffusion can be neglected) and the interaction range is finite ($Pe \to \infty$, $\beta > 0$, direct interception), a different family of approximations has been derived. In this regime, the Laplacian term in (3.6) can be neglected, and the stationary solution takes only two values: 0 inside a critical streamline and 1 outside of it. To determine Φ, one simply calculates the cross-section of the critical stream tube in the far-field flow in (3.4). This gives an expression for direct interception flux Φ_A as (Friedlander (1957), Supplementary Materials Sec. S.1)

$$\Phi_A = U\pi b^2 \frac{3-\beta}{2}\varphi_0, \tag{4.4}$$

leading to the direct interception Sherwood number

$$Sh_A = \frac{\Phi_A}{\Phi_D} = Pe\frac{\beta^2(3-\beta)}{8}. \tag{4.5}$$

It is clear that (4.3) has different asymptotics than (4.5), as the former gives $Sh_{Cl} \approx (Pe/4)^{1/3}$ when $Pe \to \infty$. Therefore, predicting encounters for fast sinking particles based on the two models depends strongly on how the limit of high Pe is approached.

To better highlight the disagreement between the two models, we consider the number of collisions Λ that occurred with a particle sedimenting over a fixed travel distance ΔZ (for example depth of the ocean). For a given diffusion coefficient D, from (4.2) we get that

$$\Lambda = \Phi_{Cl}\frac{\Delta Z}{U} = 4\pi a^2 \varphi_0 \frac{\Delta Z}{Pe} Sh_{Cl}, \tag{4.6}$$

which is vanishingly small for large Pe because, from (4.3), $Sh_{Cl} \approx (Pe/4)^{1/3}$ as $Pe \to \infty$. In other words, the advection-diffusion model in (4.3) predicts that marine snow stops intercepting new particles when it becomes fast enough ($Pe \to \infty$, by taking $U \to \infty$ with D and a constant, which can be achieved by increasing the density of the larger particle). In contrast, the number of collisions predicted by the direct interception model, (4.4), is always finite and given by $\Lambda = \varphi_0 \pi b^2 (3-\beta)\Delta Z/2$. This divergence of the predicted number of collisions between the two models arises because the advection-diffusion model assumes an infinitely small interaction range ($\beta = 0$).

Thus, for any interaction range, however small, the interaction range cannot be neglected at very large values of Pe. The true asymptotics of $Sh(Pe)$ are determined by β and, eventually, to maintain a constant, non-zero Λ from (4.6), $Sh(Pe)$ should scale as $Sh(Pe) \sim Pe$. To explore this discrepancy, we next calculate Sh numerically in the general case ($Pe \geqslant 0$ and $\beta \geqslant 0$).

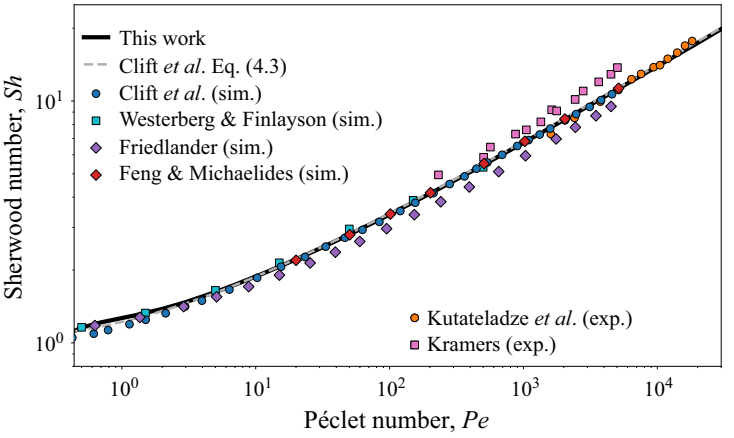

Figure 3. Validation of our numerical results in the case of zero interaction range. Comparison of our simulations with earlier experimental (Kramers 1946; Kutateladze *et al.* 1982) and numerical (Friedlander 1957; Westerberg & Finlayson 1990; Feng & Michaelides 2000; Clift *et al.* 2013) solutions of the advection-diffusion problem around a sphere in Stokes flow (thus with a zero interaction range, $\beta = 0$). Closed-form approximation of Clift *et al.* (2013) is shown as dashed line. Results from our numerical model show excellent agreement with earlier numerical works (excluding the work of Friedlander (1957) which is an outlier). Deviations from experimental data are likely driven by finite Reynolds number effects (Kramers (1946) measured *Sh* with $0.42 < Re < 26.5$). Different definitions of Péclet and Sherwood numbers were harmonised.

5. Numerical investigation

5.1. *Simulation methods*

Equation (3.6) can be solved directly using finite element method (FEM) for moderate values of Péclet number such as $1 < Pe < 10^6$. We used the Python package `scikit-fem` (Gustafsson & McBain 2020), working in cylindrical symmetry. We expressed (3.6) in a weak form and obtained solutions for the concentration profiles around the sedimenting sphere, as shown in figure 2(*b*). We provide more details on this method of solution in figure S1 in the Supplementary Materials (SM) and present convergence tests in figure S2 and figure S3 in the SM. The concentration profiles were post-processed to obtain *Sh*. We did it in two ways to further validate the numerical solution. In the first approach, we calculated Φ by integrating $Pe\,\varphi(\rho)\boldsymbol{u}(\rho)$ far downstream of the sphere. In the second approach, we calculated Φ by integrating $(Pe\,\varphi\boldsymbol{u} - \boldsymbol{\nabla}\varphi)\cdot \mathrm{d}\boldsymbol{S}$ on the surface of the capturing sphere. Whenever the simulation box was sufficiently large, these methods were in agreement (see figure S4 in the SM). For smaller values of *Pe* (e.g. $Pe \sim 0.1$) the FEM becomes impractical because it requires a very large simulation box to set the boundary conditions properly. However, this regime is well described by Sh_{Cl}, defined in (4.3).

We validated the FEM approach with solutions and experiments available in the literature for $\beta = 0$. The comparison of our numerical results for $Sh(Pe)$ is shown in figure 3. After harmonising the definitions of *Sh* and *Pe* between different sources and this publication, we see that our simulations are in good agreement with previous numerical and experimental works, and agree with the approximate relationship of (4.3).

For even higher *Pe*, FEM calculations proved ineffective due to a numerical stability problem: for very large values of *Pe*, ringing artefacts appear near sharp gradients which follow the streamlines. Refining the mesh can extend the stability of the FEM method to slightly larger values of *Pe*; similarly, more sophisticated FEM algorithms can somewhat alleviate the problems of sharp gradients. These improvements, however, are

insufficient to cover the limit of very large Pe. Since the calculations for $Pe > 10^7$ are key to understanding marine snow collisions, as seen in figure 1(*c*), we employed another simulation method.

Given that (3.5) is of Fokker–Planck type, it is possible to obtain integrals of φ by simulating the corresponding Itô stochastic differential equation (SDE) with appropriate initial and boundary conditions, as described in Van Kampen (1992) and Öttinger (1996). The simulated trajectories are used to calculate the hitting probability for a given initial position, which quantifies the number of small objects absorbed by the large particle. The total flux is then obtained by integrating the hitting probability over a disk placed upstream of the particle.

Specifically, the positions of suspended objects, $\boldsymbol{q}$, are described by the equation

$$\mathrm{d}\boldsymbol{q} = \boldsymbol{u}\mathrm{d}t + \sqrt{2D}\,\mathrm{d}\boldsymbol{W}_t, \tag{5.1}$$

with $\boldsymbol{q}(t=0) = \boldsymbol{q_0}$, and where $\boldsymbol{W}_t$ is the Wiener process. Scaling the lengths by $(a+b)$ and the time by $(a+b)/U$ leads to the dimensionless expression

$$\mathrm{d}\boldsymbol{q} = \boldsymbol{u}\mathrm{d}t + \sqrt{\frac{2}{Pe}}\,\mathrm{d}\boldsymbol{W}_t. \tag{5.2}$$

We simulated $N = 10^4$ particles for each of 50 starting points, $\boldsymbol{q_0} = (x_0, 0, -h)$, with $h = 5$, using the Python package `pychastic` (Waszkiewicz *et al.* 2023*a*, *b*). The typical resulting trajectories are shown in figure 2(*c*). The trajectories were then used to calculate the hitting probability $p_{hit}(x_0)$ as a function of x_0 for an ensemble of initial locations x_0. Specifically, $p_{hit}(x_0)$ is the fraction of trajectories that approach the particle at a distance smaller than 1. The flux Φ was calculated as

$$\Phi = \varphi_0 U (a+b)^2 \int_0^\infty 2\pi\rho\; p_{hit}(\rho)\, u_z(\rho)\,\mathrm{d}\rho. \tag{5.3}$$

To efficiently calculate the integral, we sampled p_{hit} on a non-uniform grid (figure 4; for details, see discussion of figure S5 in the SM) and used linear interpolation of p_{hit}. We note that (5.3) includes the contribution of the advective flux $(\boldsymbol{u}\varphi)$ in (3.10) and ignores the diffusive component $(D\nabla\varphi)$; This approximation utilises the fact that $\partial_z\varphi$ is negligible far downstream of the sphere.

In summary, FEM is an effective tool for simulating the dynamics of small objects for $Pe < 10^7$, while in the high-Pe regime, $Pe > 10^5$, SDE trajectories are increasingly practical due to faster convergence. We used the intermediate regime, where the two methods overlap, as a test ground to compare their results. In figure 4 we present an estimation of the hitting probability profile for $Pe = 7 \times 10^5$ and $\beta = 0.09$ using FEM and SDE. In this case, both methods converge. The details of the compatibility tests performed are included in the SM, in figure S6 and figure S7.

5.2. *Flux calculation – results*

The calculated flux Φ reveals a different asymptotic scaling with large Pe for objects with a non-zero interaction range ($\beta > 0$) compared with objects with zero interaction range ($\beta = 0$). We calculated Φ for different values of Pe and β and compared our calculations with the solution from Clift *et al.* (2013) ($\beta = 0$), given by (4.3) (figure 5*a*). We find that, for small Pe, all solutions with different β converge to the relation Sh_{Cl}. However, for higher Pe, the solutions diverge significantly from the curve with $\beta = 0$ after a transition region, eventually reaching an asymptote different from $Sh_{Cl} \approx (Pe/4)^{1/3}$. Instead, we

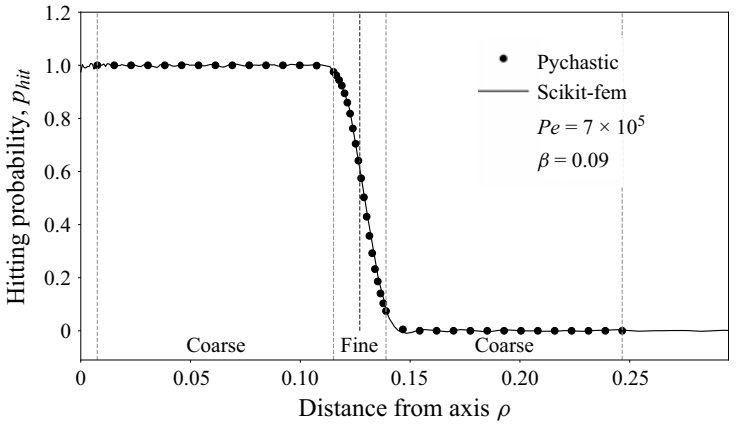

Figure 4. Hitting probability of diffusive objects with a non-zero interaction range, calculated using SDE and FEM simulations. Numerical calculations for a representative, intermediate value of Pe and β show good agreement between the FEM (`scikit-fem`) and SDE (`pychastic`) methods. In the SDE approach, each point was computed using $N = 10^4$ trajectories. To reduce computational time, a set of 50 initial conditions was chosen. In a region near the critical streamline, sampling density was increased (more details in the SM, in figure S5 and figure S6). The profile of hitting probability was used to calculate the total flux onto the particle using (5.3).

observe that the solutions for $\beta \neq 0$ approach the asymptotics of $Sh \sim Pe$ in the high-Pe limit.

To better capture the transition between the diffusion and direct interception regimes, we introduce the modified Sherwood number $\widetilde{Sh}$ as

$$\widetilde{Sh} = \frac{\Phi}{\Phi_D + \Phi_A}. \tag{5.4}$$

This extended definition ensures that all solutions for $\beta > 0$ tend to a finite limit as $Pe \to \infty$. As shown in figure 5(*b*), all numerical solutions for $\beta > 0$ eventually detach from Sh_{Cl} at a given Pe and tend to 1, thus transitioning from advection-diffusion with zero interaction range to pure direct interception. This definition thus allows us to assess the applicability of (4.3) and (4.5) simultaneously: advection-diffusion is a good estimate of the true encounter kernel as long as $\widetilde{Sh}$ is close to (4.3) and the direct interceptions approach begins to be valid, when $\widetilde{Sh}$ approaches the value of 1 for high Pe.

We provide two ways of incorporating the improved estimates of Φ for future research. First, we developed a Python package `pypesh` accompanying this manuscript which, for given Pe and β, calculates Sh as output interpolated from the calculations from figure 5(*a*). Second, we propose a closed-form approximation of the numerical results. We approximate Φ as the sum of Φ_{Cl} and Φ_A

$$\begin{aligned} Sh \approx Sh_f &= (\Phi_{Cl} + \Phi_A)/\Phi_D \\ &= Sh_{Cl} + \frac{U\pi b^2}{4\pi D(a+b)}\frac{3-\beta}{2} \\ &= \frac{1}{2}\left(1 + (1+2Pe)^{1/3} + Pe\,\frac{\beta^2(3-\beta)}{4}\right). \end{aligned} \tag{5.5}$$

Figure 5(*c*) shows the relative difference between the numerically calculated value of Sh and the approximation of (5.5). We see that Sh_f underestimates the numerical value by at most 20 %, with the maximum of deviations shifting towards higher Pe for smaller

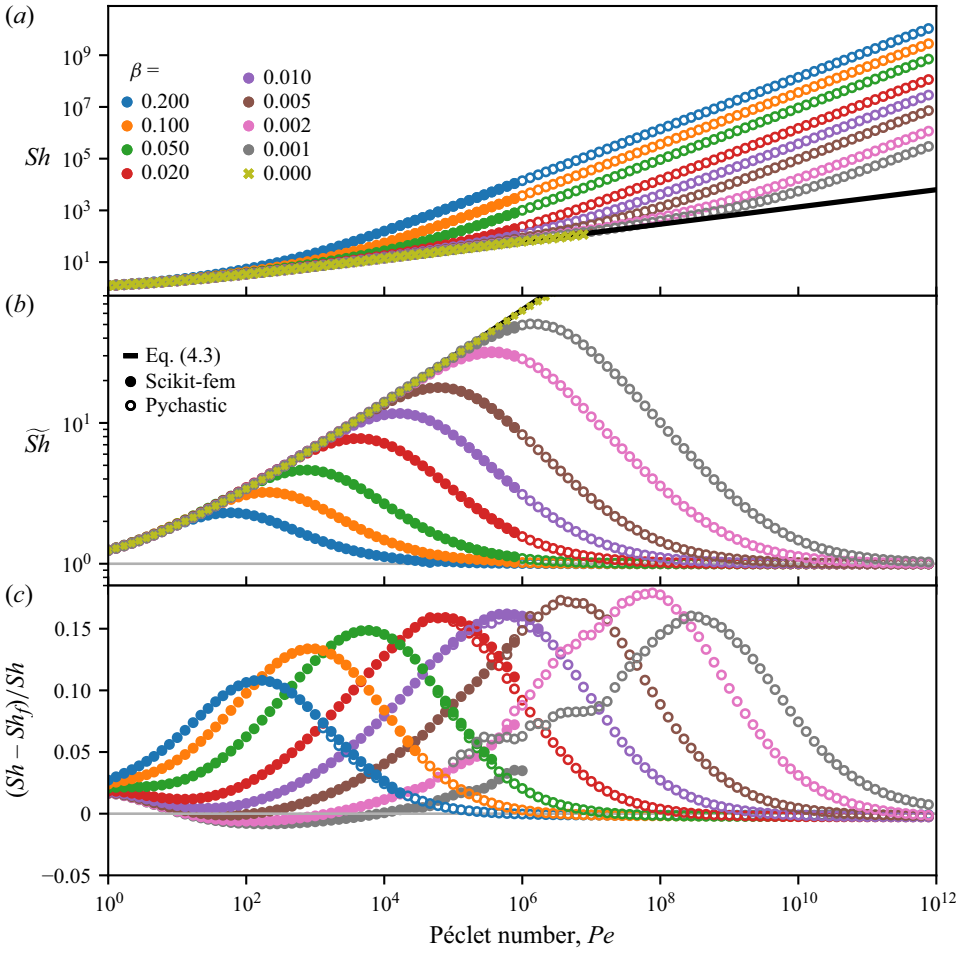

Figure 5. Sherwood number for varying Pe and β, obtained from numerical simulations. Filled dots correspond to FEM using the `scikit-fem` package, empty dots correspond to solutions of the SDE using the `pychastic` package. Colour denotes the value of β. (*a*) Sherwood number, Sh, as a function of Pe. The solutions range from ignoring the radius of objects (aligning with the solution of Clift *et al.* (2013)) to ignoring diffusion of objects (parallel straight lines in the high-Pe limit). (*b*) Results of the same calculation presented in terms of the modified Sherwood number, $\widetilde{Sh}$, defined in (5.4) . With this parametrisation, all solutions approach 1 as $Pe \to \infty$. (*c*) Relative error between numerical results for Sh and the analytical approximation Sh_f, proposed in (5.5).

values of β. We thus conclude that, the two mechanisms generating encounters – direct interception and advection-diffusion – act approximately independently. In the solution for $\beta = 0.001$, a delicate discrepancy occurs, between the two numerical schemes, caused by numerical errors of the estimated Sh. This error, however, is smaller than 5 %. In summary, the formula in (5.5) provides a closed-form approximation of the flux as a function of Pe and β.

6. Ecological implications for pico- and nanoplankton

We now apply our results to environmentally realistic scenarios. We quantify the relative contributions of advection-diffusion (4.3) and direct interception (4.4) to the total encounter kernel (5.5) as a function of the size of the suspended objects in figure 6.

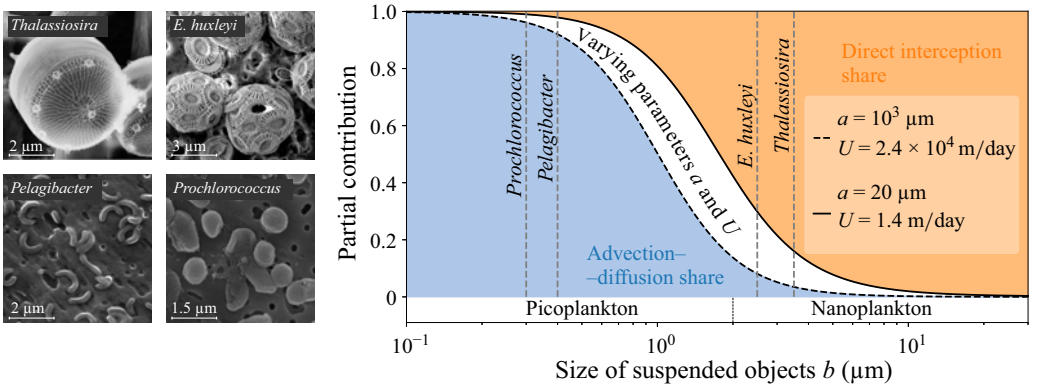

Figure 6. Advection-diffusion vs. direct interception for pico- and nanoplankton. Partial contribution to the total flux from Φ_{Cl} (denoted as the advection-diffusion share) and Φ_A (denoted as direct interception share). The white region represents a family of curves reflecting the partial contribution generated by varying $\Delta\rho$ and a ($30\,\mathrm{kg\,m^{-3}} < \Delta\rho < 200\,\mathrm{kg\,m^{-3}}$ and $20\,\mu\mathrm{m} < a < 10^3\,\mu\mathrm{m}$) in the Stokes law. An increase of $\Delta\rho$ and a leads to an increase of Φ_A in comparison with Φ_{Cl}. See figure S9 in the SM for parameterisation using smaller density differences. The vertical dashed lines represent two examples of non-motile pico- and nanoplankton each: *Prochlorococcus* (image by A. Thompson, public domain (Thompson 2009)) and *Pelagibacter* (image by L. Steindler *et al.*, CC BY 4.0 (Steindler *et al.* 2011)) as well as *E. huxleyi* (image by M. Iglesias-Rodriguez *et al.*, CC BY 4.0 (Iglesias-Rodriguez *et al.* 2017)) and *Thalassiosira* (image reproduced from Sumper & Brunner 2008 with permission).

We assume the smaller objects to be neutrally buoyant and have a diffusion coefficient described by the Stokes–Einstein relationship

$$D = \frac{k_B T}{6\pi\mu b}, \tag{6.1}$$

where $k_B = 1.38 \times 10^{-23}\,\mathrm{J\,K^{-1}}$ is the Boltzmann constant, $T = 277\,\mathrm{K}$ is the approximate temperature of seawater and $\mu = 1.6 \times 10^{-3}\,\mathrm{Pa\,s}$ is the dynamic viscosity of seawater. To calculate D for small objects, we make a common assumption that the interaction range and the size of the object are identical (Humphries 2009; Kiørboe *et al.* 2002; Jackson 1990; Burd & Jackson 2009; Alcolombri *et al.* 2025).

We assume for simplicity that larger particles sink according to the Stokes' law

$$U = \frac{2g\Delta\rho}{9\mu}a^2, \tag{6.2}$$

where $\Delta\rho$ is the density difference between water and the particles, and $g = 9.81\,\mathrm{m\,s^{-2}}$ is the gravitational acceleration. We consider a from 20 to $10^3\,\mu\mathrm{m}$ to cover a realistic range of marine snow sizes (DeVries *et al.* 2014). To mimic the variability in sinking velocities, we consider two ranges of $\Delta\rho$. First, we set $30\,\mathrm{kg\,m^{-3}} < \Delta\rho < 200\,\mathrm{kg\,m^{-3}}$ based on previously reported values (Chase 1979; McDonnell & Buesseler 2010). Second, we consider much smaller values of $\Delta\rho$ to represent slowly sinking particles.

Our formula implies that encounters between sinking marine snow and submicrometre-sized suspended objects, such as non-motile picoplankton, are driven primarily by advection-diffusion, whereas the capture mechanism for larger objects, such as non-motile nanoplankton, depends sensitively on the properties of the sinking marine snow. Figure 6 shows the relative contribution of the two terms (advective-diffusive in blue and direct interception in orange) to the total flux as a function of the size of suspended objects for the case of marine snow density differences in the range of $30\,\mathrm{kg\,m^{-3}} < \Delta\rho < 200\,\mathrm{kg\,m^{-3}}$.

In this regime, the share of advection-diffusion vs. direct interception contributions takes a sigmoidal shape, centred at approximately 1.5 μm, a location that is close to the traditional size threshold separating marine microorganisms into picoplankton and nanoplankton (Omori & Ikeda 1992). For a given size of suspended objects, the contributions of Φ_{Cl} and Φ_A are weakly dependent on the size of the marine snow particle a and vary mainly with $\Delta\rho$ (with the range of relative shares of Φ_{Cl} and Φ_A constrained by the white region; see figure S8 in the SM for more details). For example, when the smaller object has a radius of $b \approx 1$ μm, the share of advection-diffusion is between 50 % and 83 %, and the share of direct interception is between 17 % and 50 %, depending on the density of the particle. On the other hand, for $b \approx 2.5$ μm, direct interception contributes between 64 % and 91 % of the total flux. For excess density of marine snow less than $\Delta\rho = 30\,\mathrm{kg\,m^{-3}}$, the white region in figure 6 shifts towards larger values of b, while maintaining its sigmoidal shape. In the case of $\Delta\rho \approx 10^{-2}\,\mathrm{kg\,m^{-3}}$, which corresponds to $U = 1.2\,\mathrm{m\,day^{-1}}$ for $a = 10^3$ μm (such slowly sinking particles have also been observed *in situ* (Williams & Giering 2022)), the 50 % threshold on the right-hand side of figure 6 occurs at $b \approx 12$ μm (see the figure S9 in the SM for more details). This estimation shows that, as the particle slows down, direct interception may underestimate the encounter rate with suspended objects as large as nanoplankton.

7. Discussion

Estimating microhydrodynamic encounter rates is crucial for quantifying the time scales of microscale interactions (Kiørboe 2008; Burd & Jackson 2009; Słomka *et al.* 2023). In the context of marine snow particles, collisions with small suspended objects shape the dynamics of carbon export to depth by mediating the colonisation of the particles by microorganisms or the acquisition of additional ballast.

Such collisions are often quantified by the zero-interaction model ($\beta = 0$) (Kapellos *et al.* 2022; Nguyen *et al.* 2022) or by neglecting the diffusion of objects (Humphries 2009; Krishnamurthy, Pepper & Prakash 2023). However, as we have shown in § 4, the quantification of the encounter process is hampered by the different asymptotics of these two frequently used models. Through (5.5), our work provides a simple method that accurately describes both regimes and the intermediate scenarios. With an increasing number of studies determining the size distribution of marine snow particles (McCave 1984; Jackson *et al.* 1997; Bochdansky *et al.* 2016; Cavan *et al.* 2018) and their sinking speeds (Williams & Giering 2022; Chajwa *et al.* 2024), we expect our kernel to become a useful tool for assessing the importance of different encounter mechanisms on the overall sedimentation flux (Burd & Jackson 2009; Nguyen *et al.* 2022).

Importantly, we showed that considering only Pe is insufficient to rule out the contribution of diffusion to generating encounters. For example, as shown in figure 5, for $Pe = 10^6$, the direct interception model works very well when $\beta = 0.02$ (e.g. in the case of a large particle with $a \approx 175$ μm, $U \approx 20\,\mathrm{m\,day^{-1}}$, capturing small diatoms, such as *Thalassiosira*, with $b \approx 3.5$ μm). In contrast, advection-diffusion provides an almost exact result for $\beta = 0.001$ (e.g. in the case of a large particle with $a \approx 300$ μm, $U \approx 100\,\mathrm{m\,day^{-1}}$ capturing a cyanobacteria *Prochlorococcus*, $b \approx 0.3$ μm), implying that relying on direct interception alone underestimates the encounter rate by a factor of 200 in this case. Similarly, our work implies that the scavenging of neutrally buoyant biogels may occur more frequently than previously thought, possibly enhancing the slow down of sinking particles (Alcolombri *et al.* 2021), or the formation of mucus comet tails (Chajwa *et al.* 2024).

Our numerical results highlight the need to validate the *ad hoc* summation of encounter kernels. Several heuristic approaches have been proposed to describe the interception of

small objects by a large sinking particle, including using the direct interception kernel alone ((4.4) cf. Kiørboe (2001)), the sum of the direct interception and purely diffusive kernels ((4.4) and (4.1), cf. Jackson (1990); Burd & Jackson (2009)) or the sum of direct interception ((4.4) and an asymptotic variant of (4.3), valid for sufficiently large *Pe* (Shimeta & Jumars 1991; Shimeta 1993)). Here, we have shown that a specific choice of (5.5), which accounts for the summation of the direct interception and advective-diffusive kernels ((4.4) and (4.3)), provides an accurate description of encounter processes valid for all regimes. In the general case, with other collision mechanisms involved (Jackson 1990; Kriest & Evans 2000; Gehlen *et al.* 2006; Burd & Jackson 2009; Aumont *et al.* 2015; Stock *et al.* 2020), our results call for a critical assessment of the assumption of kernel additivity. Beyond models of marine snow collisions, the kernel in (5.5) may find applications in particle-laden flows relevant to atmospheric phenomena (Rosa *et al.* 2013) and industrial processes such as flotation (Jiang & Krug 2025).

Our model and its potential applications are subject to four primary limitations. First, larger, denser marine snow particles can achieve sedimentation speeds that invalidate the Stokes flow assumption (Alldredge 1998; Kiørboe *et al.* 2001), and require extension of the non-zero *Re* model of Humphries (2009) to include the diffusion of objects. Second, our approach neglects hydrodynamic interactions that become relevant when the sizes of colliders are comparable or when the smaller collider is sufficiently large to exert non-negligible impact on the flow, and can be accounted for by including the distance-dependent hydrodynamic mobility of two spheres (Jeffrey & Onishi 1984; Lisicki *et al.* 2014). Third, we have assumed non-motile objects. Motility can be incorporated using effective diffusion (Lambert *et al.* 2019) in the case of large marine snow, whereas encounters with smaller marine snow must take into account the reorienting effects of the shear profile on motile cells (Słomka *et al.* 2020). Finally, we assumed effective spherical shapes of the sinking particles. While marine snow particles have irregular shapes and calculating encounter rates for a given shape of a collider remains largely an open question, we consider here an effective hydrodynamic radius and expect that the primary role of the shape is to determine the particle's sinking speed. In amorphous cases, we expect the demarcation between advective-diffusive and ballistic encounters predicted by (5.5) to hold more broadly.

8. Conclusions

In this study, we theoretically and numerically addressed the problem of quantifying encounters between a large sinking sphere and suspended objects, depending on the size and sinking speed of the large sphere, as well as the size and diffusivity of the objects. Using advection-diffusion simulations, based on the FEM and SDE approaches, we quantified the encounter rate for a wide range of parameters of the colliding objects. The results are succinctly described by a compact formula for the resulting encounter kernel, (5.5), which can be used to rapidly estimate encounter rates as a function of two dimensionless groups, the Péclet number *Pe* and β, the relative size of the objects and the large particle. In the context of marine snow, our work implies that advection-diffusion often remains the main driver of encounters with plankton and gels, even at very high Péclet numbers. Overall, by improving estimates of encounter rates, our results can inform models of carbon cycling in ocean ecosystems.

Supplementary material. Supplementary materials are available at https://doi.org/10.1017/jfm.2026.11282.

Acknowledgements. The authors thank Dr E. Trudnowska for sharing images of marine particulate matter and insightful comments. Fenix Science Club is acknowledged for providing computational power.

Funding. The work was supported by a Swiss NSF Ambizione grant no. PZ00P2_202188 to J.S., and the National Science Centre of Poland Sonata Bis grant no. 2023/50/E/ST3/00465 to M.L.

Declaration of interests. The authors report no conflicts of interest.

Data availability statement. All the software used in the above simulations is open source with an open licence and can be accessed from our repositories on Github (Turczynowicz & Waszkiewicz 2024) and Zenodo (Waszkiewicz & Turczynowicz 2025). Additionally, as mentioned earlier, the Python package `pypesh` accompanies this manuscript. This package interpolates the *Sh* values from the calculations presented in figure 5 or performs direct computations for given parameters.

References

Acrivos, A. & Goddard, J.D. 1965 Asymptotic expansions for laminar forced-convection heat and mass transfer. Part 1. Low speed flows. *J. Fluid Mech.* **23**, 273–291.

Acrivos, A. & Taylor, T.D. 1962 Heat and mass transfer from single spheres in Stokes flow. *Phys. Fluids* **5** (4), 387–394.

Alcolombri, U., *et al.* 2025 Biogel scavenging slows the sinking of organic particles to the ocean depths. *Nat. Commun.* **16** (1), 3290.

Alcolombri, U., Peaudecerf, F.J., Fernandez, V.I., Behrendt, L., Lee, K.S. & Stocker, R. 2021 Sinking enhances the degradation of organic particles by marine bacteria. *Nat. Geosci.* **14** (10), 775–780.

Alldredge, A. 1998 The carbon, nitrogen and mass content of marine snow as a function of aggregate size. *Deep Sea Res. Part I: Oceanograph. Res. Papers* **45** (4-5), 529–541.

Anderson, T.R., Gentleman, W.C., Cael, B.B., Hirschi, J.J.-M., Eastwood, R.L. & Mayor, D.J. 2023 Proliferating particle surface area via microbial decay has profound consequences for remineralisation rate: a new approach to modelling the degradation of sinking detritus in the ocean. *Biogeochemistry* **164** (2), 335–347.

Armstrong, R.A., Lee, C., Hedges, J.I., Honjo, S. & Wakeham, S.G. 2001 A new, mechanistic model for organic carbon fluxes in the ocean based on the quantitative association of POC with ballast minerals. *Deep Sea Res. Part II: Topical Stud. Oceanogr.* **49** (1), 219–236.

Aumont, O., Ethé, C., Tagliabue, A., Bopp, L. & Gehlen, M. 2015 PISCES-v2: an ocean biogeochemical model for carbon and ecosystem studies. *Geosci. Model Dev.* **8** (8), 2465–2513.

Bell, C.G., Byrne, H.M., Whiteley, J.P. & Waters, S.L. 2013 Heat or mass transfer from a sphere in Stokes flow at low Péclet number. *Appl. Math. Lett.* **26** (4), 392–396.

Bochdansky, A.B., Clouse, M.A. & Herndl, G.J. 2016 Dragon kings of the deep sea: marine particles deviate markedly from the common number-size spectrum. *Sci. Rep.* **6** (1), 22633.

Boyd, P.W., Claustre, H., Levy, M., Siegel, D.A. & Weber, T. 2019 Multi-faceted particle pumps drive carbon sequestration in the ocean. *Nature* **568** (7752), 327–335.

Briggs, N., Dall'Olmo, G. & Claustre, H. 2020 Major role of particle fragmentation in regulating biological sequestration of CO_2 by the oceans. *Science* **367** (6479), 791–793.

Broecker, W.S. & Peng, T.-H. 1982 *Tracers in the Sea*. Lamont-Doherty Geological Observatory, Columbia University.

Brunn, P.O. 1982 Heat or mass transfer from single spheres in a low Reynolds number flow. *Intl J. Engng Sci.* **20** (7), 817–822.

Buesseler, K.O. & Boyd, P.W. 2009 Shedding light on processes that control particle export and flux attenuation in the twilight zone of the open ocean. *Limnol. Oceanogr.* **54** (4), 1210–1232.

Buesseler, K.O., Boyd, P.W., Black, E.E. & Siegel, D.A. 2020 Metrics that matter for assessing the ocean biological carbon pump. *Proc. Natl Acad. Sci. USA* **117**, 9679–9687.

Buesseler, K.O., Lamborg, C.H., Boyd, P.W., Lam, P.J., Trull, T.W., Bidigare, R.R., Bishop, J.K.B., Casciotti, K.L., Dehairs, F. & Elskens, M. 2007 Revisiting carbon flux through the ocean's twilight zone. *Science* **316** (5824), 567–570.

Burd, A.B. & Jackson, G.A. 2009 Particle aggregation. *Annu. Rev. Mar. Sci.* **1** (1), 65–90.

Cael, B.B., *et al.* 2021 Open ocean particle flux variability from surface to seafloor. *Geophys. Res. Lett.* **48** (9), e2021GL092895.

Cavan, E.L., Giering, S.L.C., Wolff, G.A., Trimmer, M. & Sanders, R. 2018 Alternative particle formation pathways in the eastern tropical north pacific's biological carbon pump. *J. Geophys. Res.: Biogeosci.* **123** (7), 2198–2211.

Chajwa, R., Flaum, E., Bidle, K.D., Mooy, B.V. & Prakash, M. 2023, Hidden Comet-Tails of Marine Snow Impede Ocean-based Carbon Sequestration. arXiv: 2310.01982.

CHAJWA, R., FLAUM, E., BIDLE, K.D., VAN MOOY, B. & PRAKASH, M. 2024 Hidden comet tails of marine snow impede ocean-based carbon sequestration. *Science* **386** (6718), eadl5767.

CHASE, R.R.P. 1979 Settling behavior of natural aquatic particulates. *Limnol. Oceanogr.* **24** (3), 417–426.

CLEMENTS, D.J., YANG, S., WEBER, T., MCDONNELL, A.M.P., KIKO, R., STEMMANN, L. & BIANCHI, D. 2022 Constraining the particle size distribution of large marine particles in the global ocean with in situ optical observations and supervised learning. *Glob. Biogeochem. Cycles* **36** (5), e2021GB007276.

CLIFT, R., GRACE, J.R. & WEBER, M.E. 2013 *Bubbles, Drops, and Particles*. Courier Corporation.

DEVRIES, T., LIANG, J.-H. & DEUTSCH, C. 2014 A mechanistic particle flux model applied to the oceanic phosphorus cycle. *Biogeosciences* **11** (19), 5381–5398.

DILLING, L. & ALLDREDGE, A.L. 2000 Fragmentation of marine snow by swimming macrozooplankton: a new process impacting carbon cycling in the sea. *Deep Sea Res. Part I: Oceanogr. Res. Papers* **47** (7), 1227–1245.

DURET, M. 2018 Microbial communities in sinking and suspended particles and their influence on the oceanic biological carbon pump. PhD thesis, University of Southampton.

FENG, Z. & MICHAELIDES, E.E. 2000 Mass and heat transfer from fluid spheres at low Reynolds numbers. *Powder Technol.* **112** (1-2), 63–69.

FRIEDLANDER, S.K. 1957 Mass and heat transfer to single spheres and cylinders at low Reynolds numbers. *AIChE J.* **3** (1), 43–48.

GEHLEN, M., BOPP, L., EMPRIN, N., AUMONT, O., HEINZE, C. & RAGUENEAU, O. 2006 Reconciling surface ocean productivity, export fluxes and sediment composition in a global biogeochemical ocean model. *Biogeosciences* **3** (4), 521–537.

GIERING, S.L.C., SANDERS, R., MARTIN, A.P., HENSON, S.A., RILEY, J.S., MARSAY, C.M. & JOHNS, D.G. 2017 Particle flux in the oceans: challenging the steady state assumption. *Glob. Biogeochem. Cycles* **31** (1), 159–171.

GUIDI, L., *et al.* 2016 Plankton networks driving carbon export in the oligotrophic ocean. *Nature* **532** (7600), 465–470.

GUPALO, Y.P. & RYAZANTSEV, Y.S. 1972 Mass and heat transfer from a sphere in a laminar flow. *Chem. Engng Sci.* **27** (1), 61–68.

GUSTAFSSON, T. & MCBAIN, G.D. 2020 scikit-fem: a python package for finite element assembly. *J. Open Source Softw.* **5** (52), 2369.

HUMPHRIES, S. 2009 Filter feeders and plankton increase particle encounter rates through flow regime control. *Proc. Natl Acad. Sci.* **106** (19), 7882–7887.

IGLESIAS-RODRIGUEZ, M.D., JONES, B.M., BLANCO-AMEIJEIRAS, S., GREAVES, M., HUETE-ORTEGA, M. & LEBRATO, M. 2017 Physiological responses of coccolithophores to abrupt exposure of naturally low pH deep seawater. *PLOS One* **12** (7), 1–20.

IVERSEN, M.H., NOWALD, N., PLOUG, H., JACKSON, G.A. & FISCHER, G. 2010 High resolution profiles of vertical particulate organic matter export off Cape Blanc, Mauritania: degradation processes and ballasting effects. *Deep Sea Res. Part I: Oceanogr. Res. Papers* **57** (6), 771–784.

IVERSEN, M.H. & PLOUG, H. 2010 Ballast minerals and the sinking carbon flux in the ocean: carbon-specific respiration rates and sinking velocity of marine snow aggregates. *Biogeosciences* **7** (9), 2613–2624.

IVERSEN, M.H. & PLOUG, H. 2013 Temperature effects on carbon-specific respiration rate and sinking velocity of diatom aggregates–potential implications for deep ocean export processes. *Biogeosciences* **10** (6), 4073–4085.

JACKSON, G.A. 1990 A model of the formation of marine algal flocs by physical coagulation processes. *Deep Sea Res. Part A. Oceanogr. Res. Papers* **37** (8), 1197–1211.

JACKSON, G.A., MAFFIONE, R., COSTELLO, D.K., ALLDREDGE, A.L., LOGAN, B.E. & DAM, H.G. 1997 Particle size spectra between 1 μm and 1 cm at Monterey Bay determined using multiple instruments. *Deep Sea Res. Part I: Oceanogr. Res. Papers* **44** (11), 1739–1767.

JANG, G., HONG, S., OH, J., KIM, Y.-IL, KIM, M. & LEE, H. 2024 Statistical analysis of the association between El Niño and the biological carbon pump in the East Sea (Japan Sea). *Sci. Rep.* **14** (1), 26582.

JEFFREY, D.J. & ONISHI, Y. 1984 Calculation of the resistance and mobility functions for two unequal rigid spheres in low-Reynolds-number flow. *J. Fluid Mech.* **139**, 261–290.

JIANG, L. & KRUG, D. 2025 How turbulence increases the bubble–particle collision rate. *J. Fluid Mech.* **1006**, A19.

KAJIHARA, M. 1971 Settling velocity and porosity of large suspended particle. *J. Oceanogr. Soc. Japan* **27** (4), 158–162.

KAPELLOS, G.E., EBERL, H.J., KALOGERAKIS, N., DOYLE, P.S. & PARASKEVA, C.A. 2022 Impact of microbial uptake on the nutrient plume around marine organic particles: high-resolution numerical analysis. *Microorganisms* **10**, 10.

KARP-BOSS, L., BOSS, E. & JUMARS, P.A. 1996 Nutrient fluxes to planktonic osmotrophs in the presence of fluid motion. *Oceanogr. Mar. Biol.* **34**, 71–108.
KIØRBOE, T. 2001 Formation and fate of marine snow: small-scale processes with large-scale implications. *Sci. Mar.* **65** (S2), 57–71.
KIØRBOE, T., GROSSART, H.-P., PLOUG, H. & TANG, K. 2002 Mechanisms and rates of bacterial colonization of sinking aggregates. *Appl. Environ. Microb.* **68** (8), 3996–4006.
KIØRBOE, T. & TITELMAN, J. 1998 Feeding, prey selection and prey encounter mechanisms in the heterotrophic dinoflagellate *Noctiluca scintillans*. *J. Plankton Res.* **20** (8), 1615–1636.
KIØRBOE, T. 2008 *A Mechanistic Approach to Plankton Ecology*. Princeton University Press.
KIØRBOE, T., PLOUG, H. & THYGESEN, U.H. 2001 Fluid motion and solute distribution around sinking aggregates. I. Small-scale fluxes and heterogeneity of nutrients in the pelagic environment. *Mar. Ecol. Prog. Ser.* **211**, 1–13.
KIØRBOE, T. & THYGESEN, U. 2001 Fluid motion and solute distribution around sinking aggregates. II. Implications for remote detection by colonizing zooplankters. *Mar. Ecol.* **211**, 15–25.
KRAMERS, H. 1946 Heat transfer from spheres to flowing media. *Physica* **12** (2-3), 61–80.
KRIEST, I. & EVANS, G.T. 2000 A vertically resolved model for phytoplankton aggregation. *J. Earth Syst. Sci.* **109** (4), 453–469.
KRISHNAMURTHY, D., PEPPER, R. & PRAKASH, M. 2023 Active sinking particles: sessile suspension feeders significantly alter the flow and transport to sinking aggregates. *J. R. Soc. Interface* **20** (199), 20220537.
KUTATELADZE, S.S., NAKORYAKOV, V.E. & ISKAKOV, M.S. 1982 Electrochemical measurements of mass transfer between a sphere and liquid in motion at high Péclet numbers. *J. Fluid Mech.* **125**, 453–462.
LAMBERT, B.S., FERNANDEZ, V.I. & STOCKER, R. 2019 Motility drives bacterial encounter with particles responsible for carbon export throughout the ocean. *Limnol. Oceanogr. Lett.* **4** (5), 113–118.
LANDAU, L.D. & LIFSHITZ, E.M. 1987 *Fluid Mechanics, Second Edition: Volume 6 (Course of Theoretical Physics)*. Butterworth-Heinemann.
LAUFKÖTTER, C., JOHN, J.G., STOCK, C.A. & DUNNE, J.P. 2017 Temperature and oxygen dependence of the remineralization of organic matter. *Glob. Biogeochem. Cycles* **31** (7), 1038–1050.
LISICKI, M., CICHOCKI, B., ROGERS, S.A., DHONT, J.K.G. & LANG, P.R. 2014 Translational and rotational near-wall diffusion of spherical colloids studied by evanescent wave scattering. *Soft Matt.* **10** (24), 4312.
MARSAY, C.M., SANDERS, R.J., HENSON, S.A., PABORTSAVA, K., ACHTERBERG, E.P. & LAMPITT, R.S. 2015 Attenuation of sinking particulate organic carbon flux through the mesopelagic ocean. *Proc. Natl Acad. Sci.* **112** (4), 1089–1094.
MARTIN, J.H., KNAUER, G.A., KARL, D.M. & BROENKOW, W.W. 1987 VERTEX: carbon cycling in the northeast pacific. *Deep Sea Res. Part A. Oceanogr. Res. Papers* **34** (2), 267–285.
MCCAVE, I.N. 1984 Size spectra and aggregation of suspended particles in the deep ocean. *Deep Sea Res. Part A. Oceanogr. Res. Papers* **31** (4), 329–352.
MCDONNELL, A.M.P. & BUESSELER, K.O. 2010 Variability in the average sinking velocity of marine particles. *Limnol. Oceanogr.* **55** (5), 2085–2096.
MIDDELBURG, J.J. 2019 *Marine Carbon Biogeochemistry: A Primer for Earth System Scientists*. Springer International Publishing.
NGUYEN, T.T.H., *et al.* 2022 Microbes contribute to setting the ocean carbon flux by altering the fate of sinking particulates. *Nat. Commun.* **13** (1), 1657.
OLLI, K. 2015 Unraveling the uncertainty and error propagation in the vertical flux Martin curve. *Prog. Oceanogr.* **135**, 146–155.
OMAND, M.M., GOVINDARAJAN, R., HE, J. & MAHADEVAN, A. 2020 Sinking flux of particulate organic matter in the oceans: sensitivity to particle characteristics. *Sci. Rep.* **10** (1), 5582.
OMORI, M. & IKEDA, T. 1992 *Methods in Marine Zooplankton Ecology*. Krieger Publishing Company.
ÖTTINGER, H.C. 1996 *Stochastic Processes in Polymeric Fluids: Tools and Examples for Developing Simulation Algorithms*. Springer.
RIMMER, P.L. 1968 Heat transfer from a sphere in a stream of small Reynolds number. *J. Fluid Mech.* **32** (1), 1–7.
ROSA, B., PARISHANI, H., AYALA, O., GRABOWSKI, W.W. & WANG, L.-P. 2013 Kinematic and dynamic collision statistics of cloud droplets from high-resolution simulations. *New J. Phys.* **15** (4), 045032.
SABINE, C.L., FEELY, R.A., GRUBER, N., KEY, R.M., LEE, K., BULLISTER, J.L., WANNINKHOF, R., WONG, C.S.L., WALLACE, D.W.R. & TILBROOK, B. 2004 The oceanic sink for anthropogenic CO_2. *Science* **305** (5682), 367–371.
SARMIENTO, J.L. & GRUBER, N. 2006 *Ocean Biogeochemical Dynamics*. Princeton University Press.
SHIMETA, J. 1993 Diffusional encounter of submicrometer particles and small cells by suspension feeders. *Limnol. Oceanogr.* **38** (2), 456–465.

SHIMETA, J. & JUMARS, P. 1991 Physical mechanisms and rates of particle capture by suspension-feeders. *Oceanogr. Mar. Biol.: Ann. Rev.* **29**, 29.

SMITH, K.L., RUHL, H.A., HUFFARD, C.L., MESSIÉ, M. & KAHRU, M. 2018 Episodic organic carbon fluxes from surface ocean to abyssal depths during long-term monitoring in NE Pacific. *Proc. Natl Acad. Sci.* **115** (48), 12235–12240.

STEINDLER, L., SCHWALBACH, M.S., SMITH, D.P., CHAN, F. & GIOVANNONI, S.J. 2011 Energy starved, *candidatus*, pelagibacter ubique substitutes light-mediated ATP production for endogenous carbon respiration. *PLOS One* **6**, 1–10.

STOCK, C.A., DUNNE, J.P., FAN, S., GINOUX, P., JOHN, J., KRASTING, J.P., LAUFKÖTTER, C., PAULOT, F. & ZADEH, N. 2020 Ocean biogeochemistry in GFDL's earth system model 4.1 and its response to increasing atmospheric CO_2. *J. Adv. Model. Earth Syst.* **12** (10), e2019MS002043.

SUMPER, M. & BRUNNER, E. 2008 Silica biomineralisation in diatoms: the model organism thalassiosira pseudonana. *ChemBioChem* **9** (8), 1187–1194.

SŁOMKA, J., ALCOLOMBRI, U., CARRARA, F., FOFFI, R., PEAUDECERF, F.J., ZBINDEN, M. & STOCKER, R. 2023 Encounter rates prime interactions between microorganisms. *Interface Focus* **13** (2), 20220059.

SŁOMKA, J., ALCOLOMBRI, U., SECCHI, E., STOCKER, R. & FERNANDEZ, V.I. 2020 Encounter rates between bacteria and small sinking particles. *New J. Phys.* **22** (4), 043016.

TAKEUCHI, M., GIERING, S.L.C. & YAMAZAKI, H. 2024 Size distribution of aggregates across different aquatic systems around Japan shows that stronger aggregates are formed under turbulence. *Limnol. Oceanogr.* **69** (11), 2580–2595.

THOMPSON, A. 2009 Prochlorococcus MIT9215 SEM, Chisholm lab. Available at https://www.flickr.com/photos/prochlorococcus/3288824796/.

TRUDNOWSKA, E., LACOUR, L., ARDYNA, M., ROGGE, A., IRISSON, J.O., WAITE, A.M., BABIN, M. & STEMMANN, L. 2021 Marine snow morphology illuminates the evolution of phytoplankton blooms and determines their subsequent vertical export. *Nat. Commun.* **12** (1), 2816.

TURCZYNOWICZ, J. & WASZKIEWICZ, R. 2024 Pypesh: advection diffusion solver. Available at: https://github.com/turczyneq/pypesh.

VAN, K. & GODFRIED, N. 1992 *Stochastic Processes in Physics and Chemistry*, vol. 1. Elsevier.

WASZKIEWICZ, R., BARTCZAK, M., KOLASA, K. & LISICKI, M. 2023*a* Codebase release 0.2 for Pychastic. *SciPost Phys. Codebases* 11–r0.2.

WASZKIEWICZ, R., BARTCZAK, M., KOLASA, K. & LISICKI, M. 2023*b* Pychastic: precise Brownian dynamics using Taylor-Itō integrators in Python. *SciPost Phys. Codebases* 11.

WASZKIEWICZ, R. & TURCZYNOWICZ, J. 2025 Pypesh solver. Zenedo. Available at: https://doi.org/10.5281/zenodo.15031242.

WESTERBERG, K.W. & FINLAYSON, B.A. 1990 Heat transfer to spheres from a polymer melt. *Numer. Heat Trans.* **17** (3), 329–348.

WILLIAMS, J.R. & GIERING, S.L.C. 2022 In situ particle measurements deemphasize the role of size in governing the sinking velocity of marine particles. *Geophys. Res. Lett.* **49** (21), e2022GL099563.

ZACCONE, A., GENTILI, D., WU, H. & MORBIDELLI, M. 2010 Shear-induced reaction-limited aggregation kinetics of brownian particles at arbitrary concentrations. *J. Chem. Phys.* **132** (13), 134903.